Topological nodal-line semimetals in alkaline-earth stannides, germanides, and silicides

Huaqing Huang, Jianpeng Liu, David Vanderbilt, and Wenhui Duan

Phys. Rev. B **93**, 201114 — Published 26 May 2016

DOI: 10.1103/PhysRevB.93.201114

Topological nodal-line semimetals in alkaline-earth stannides, germanides and silicides

Huaqing Huang,[1,2] Jianpeng Liu,[3,4] David Vanderbilt,[4] and Wenhui Duan[a1,2,5]

[1]*Department of Physics and State Key Laboratory of Low-Dimensional Quantum Physics, Tsinghua University, Beijing 100084, China*

[2]*Collaborative Innovation Center of Quantum Matter, Tsinghua University, Beijing 100084, China*

[3]*Kavli Institute for Theoretical Physics, University of California, Santa Barbara, California 93106, USA*

[4]*Department of Physics and Astronomy, Rutgers University, Piscataway, New Jersey 08854-8019, USA*

[5]*Institute for Advanced Study, Tsinghua University, Beijing 100084, China*

(Dated: May 11, 2016)

Abstract

Based on first-principles calculations and an effective Hamiltonian analysis, we systematically investigate the electronic and topological properties of alkaline-earth compounds AX_2 ($A =$ Ca, Sr, Ba; $X =$ Si, Ge, Sn). Taking $BaSn_2$ as an example, we find that when spin-orbit coupling is ignored, these materials are three-dimensional topological nodal-line semimetals characterized by a snake-like nodal loop in three-dimensional momentum space. Drumhead-like surface states emerge either inside or outside the loop circle on the (001) surface depending on surface termination, while complicated double-drumhead-like surface states appear on the (010) surface. When spin-orbit coupling is included, the nodal line is gapped and the system becomes a topological insulator with Z_2 topological invariants (1;001). Since spin-orbit coupling effects are weak in light elements, the nodal-line semimetal phase is expected to be achievable in some alkaline-earth germanides and silicides.

[a] dwh@phys.tsinghua.edu.cn

Introduction. The discoveries of topological insulators [1, 2] and Chern insulators [3–6] have attracted broad interest to topological aspects of band theory. These topologically nontrivial materials are bulk insulators with novel gapless edge or surface states protected by bulk band topology. Recently it has been shown that certain types of bulk semimetallic systems may also possess non-trivial topological properties such as topologically protected gapless surface states. These topological semimetallic states are characterized by band touching (BT) points or lines between valence and conduction bands in three-dimensional (3D) momentum space. Up to now, three types of topologically nontrivial semimetals have been proposed: Dirac [7], Weyl [8] and nodal-line semimetals [9–16]. Weyl and Dirac semimetals exhibit two-fold and four-fold degenerate BT points near the Fermi level respectively, and their low-energy bulk excitations are linearly dispersing Weyl or Dirac fermions. Unlike Weyl and Dirac semimetals with isolated bulk BT points, topological nodal-line semimetals possess BTs along one-dimensional (1D) loops or lines in 3D momentum space.

So far, significant progress has been made in identifying topological semimetals in realistic materials. For example, the Dirac-semimetal state in Na_3Bi and Cd_3As_2 [7] and Weyl-semimetal state in the TaAs family of compounds [8] have been predicted theoretically and then verified by experiments. A few candidate materials for topological nodal-line semimetals have also been proposed recently. Depending on the degeneracy of the states along the loop, these materials can be classified into two groups. One is known as the Dirac-type nodal-line semimetal, in which two doubly degenerate bands cross each other to form a four-fold degenerate nodal loop. This kind of nodal-line semimetal can typically be realized in materials with both inversion and time reversal symmetries when spin-orbit coupling (SOC) is neglected and band inversion happens around one or more high-symmetry points in Brillouin zone (BZ). The other one lacks either inversion or time-reversal symmetry, so that the otherwise four-fold degenerate nodal loops are split into two doubly degenerate nodal loops, called "Weyl nodal lines" in the literature [16]. These nodal lines are usually protected by additional crystalline symmetries such as mirror reflection so as to be stable against perturbations, including SOC.

In the present work, based on first-principles calculations and a model Hamiltonian analysis, we find a topological nodal-line semimetal phase in the alkaline-earth compound AX_2 ($A =$ Ca, Sr, Ba; $X =$ Si, Ge, Sn) when SOC is absent. Unlike the existing nodal-line semimetal materials, this system exhibits a snake-like nodal loop in 3D momentum space.

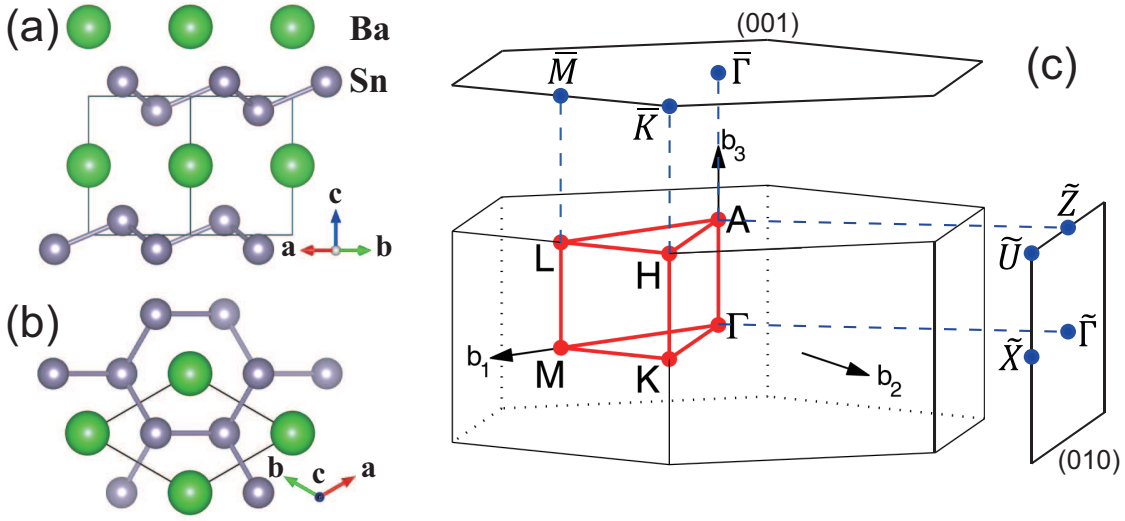

FIG. 1. (Color online) (a)-(b) Crystal structure of $BaSn_2$ with $P\bar{3}m1$ symmetry. (c) Brillouin zone of the bulk and the projected surface Brillouin zones of the (001) and (010) surfaces.

More interestingly, dispersive gapless surface states exist on the (001) surface, while some special double-drumhead-like surface states occur on the (010) surface. Including SOC in the first-principles calculation leads to a transition from a nodal-line semimetal to a strong topological insulator with (1;001) Z_2 indices. Since the SOC effect is negligible in silicides and remains small in germanides, the nodal-line semimetal phase is expected to be realized in these compounds.

Crystal structure and methodology. Since the compounds in the AX_2 family have similar centrosymmetric crystal structures and electronic structures, we take $BaSn_2$, which has been synthesized successfully [17, 18], as an example hereafter. $BaSn_2$ crystallizes in the trigonal $P\bar{3}m1$ structure (space group No. 164) as shown in Fig. 1. In this structure, the Sn atoms form a buckled honeycomb lattice, while each hexagonal Ba layer intercalates between two neighboring Sn layers.

In order to understand the electronic structure of the AX_2 compounds, we perform first-principles calculations within the framework of density-functional theory as implemented in the Vienna *ab initio* simulation package [19] with the projector augmented-wave method [20]. The Perdew-Burke-Ernzerhof exchange-correlation funcional in the generalized gradient approximation is adopted [21]. The kinetic energy cutoff is fixed to 520 eV and an 8×8×8 Γ-centered **k** mesh is used for the BZ sampling. The electronic structure is calculated both with and without SOC. We also generate *ab initio* tight-binding Hamiltonians in the basis of

projected atomic-like Wannier functions without applying a maximal-localization procedure [22, 23]. In the Wannier representation, we calculate the surface states using the iterative Green's function method [24] based on the bulk tight-binding model neglecting possible surface reconstructions and charge rearrangements. The topological feature of the surface states are expected to be captured by such simplified Wannier-based approach [25].

Electronic structures. We first study the electronic structure of $BaSn_2$ in the absence of SOC. The band structure along the high-symmetry path marked by red lines in Fig. 1(c) is shown in Fig. 2(a). It can be seen that there is a BT close to the Fermi level along the A-H line. Since the lowest conduction band and the highest valence band along this line have opposite parities with respect to the C_2 operation in the little group of A-H, they can touch each other without opening a gap. Further orbital-character analysis reveals that the states around the Fermi level are dominated by Sn s and Sn p_z orbitals, as shown in Fig. 2(a). Moreover, there is a clear signature of band inversion at the A point, implying possible non-trivial band topology. It should be noted that the band inversion at the A point is not due to SOC as it is excluded in this calculation.

Although the linear dispersion around the BT resembles the character of a Dirac semimetal, the system is actually a nodal-line semimetal. Namely, the BT persists along a closed loop in the 3D BZ forming a snake-like nodal loop around the A point. If the loop were exactly constant in energy, the iso-energy surfaces would shrink to become exactly this loop at the energy of the loop. While the energy of the BT varies slightly along the loop, its shape is still easily inferred by looking at an isoenergy countour at an energy slightly above that of the loop. Such a contour, plotted at 25 meV above the Fermi energy E_F, is shown in Fig. 2(b)-2(d). Given that the BZ is periodic, the calculated isoenergy surface forms a a closed snake-like pipe enclosing the nodal line which in turn winds around the A point. Thus, there is a single nodal loop in the BZ.

Further fine band structure calculations within the 1/6 BZ using Wannier interpolation indicate that the nodal loop has its maximum energy of 0.117 eV when passing through the Γ-M-L-A plane at $(0.136, 0.0, 0.707)$ (in units of $(2\pi/a, 2\pi/a, 2\pi/c)$), and its minimum of 0.064 eV when passing through the A-H line at (0.064, 0.064, 0.5). The energy then increases back to 0.117 eV as the loop snakes to $(0.0, 0.136, 0.293)$ on the adjacent k_y-k_z plane, and the remaining 5/6 of the loop is related to this segment by symmetries. $BaSn_2$ is unusual in having just a single loop, whereas other nodal-loop systems such as $Cu_3NPd(Zn)$ [13] and

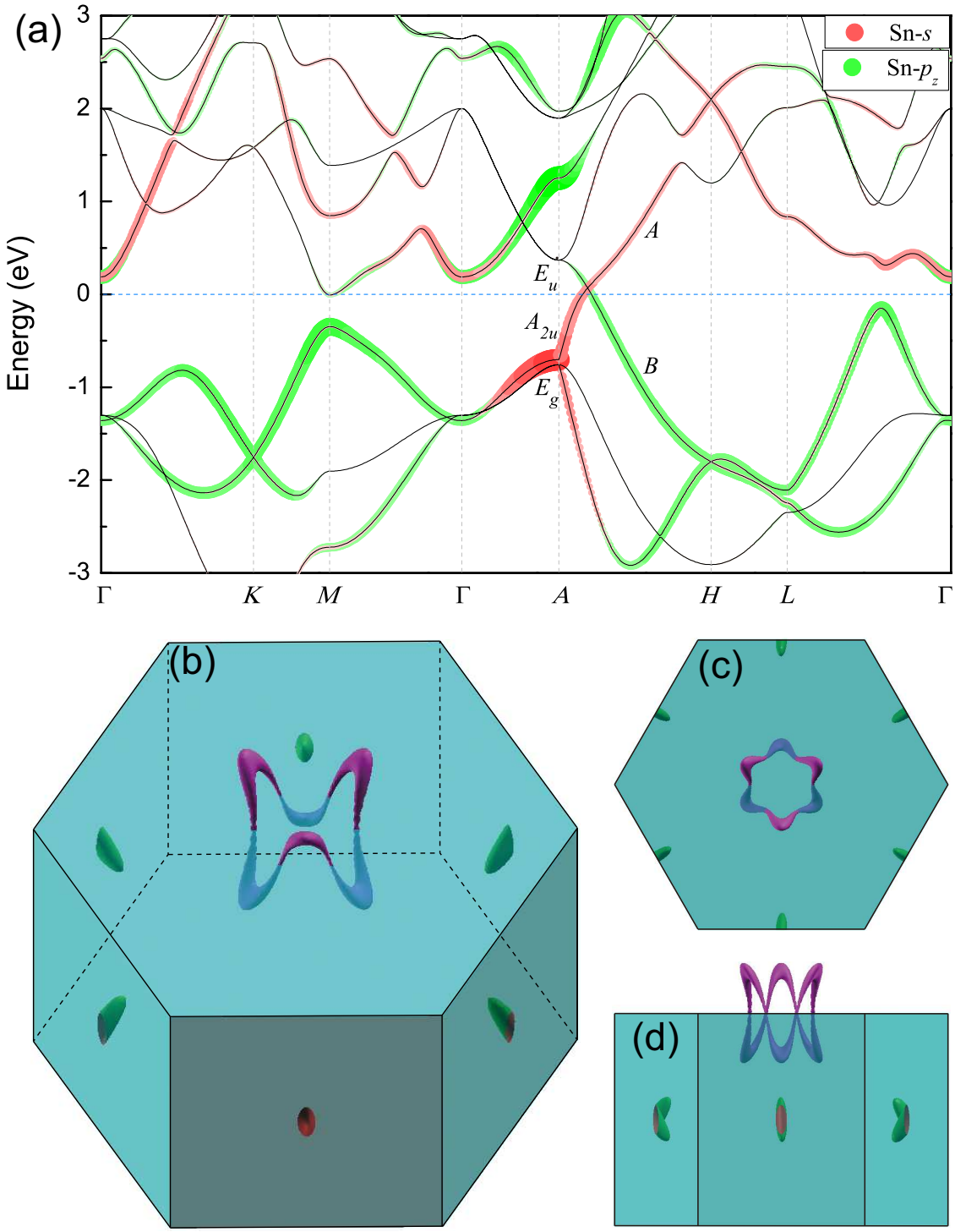

FIG. 2. (Color online) (a) Calculated band structure without SOC. The irreducible representation of selected bands at A and along A-H line are indicated. Red and green dots in band structures indicate the projection to the Sn s and p_z orbital, respectively. (b) Corresponding 3D iso-energy surface at $E = E_F + 25\,\text{meV}$. (c) Top view and (d) side view of the isoenergy surface from the (001) and (010) directions of the Brillouin zone, respectively.

$Pb(Tl)TaSe_2$ [14] typically have multiple circles or ellipses. Moreover, despite three small electron pockets around the M point, the Fermi surface is mostly contributed by the single nodal loop, which makes it easier to study any intriguing properties related to the presence of the nodal loop.

Symmetry analysis. The nodal loop in $BaSn_2$ is topologically protected due to the coexistence of time-reversal ($\mathcal{T}$) and spatial inversion ($\mathcal{P}$) symmetries [12, 26]. When SOC is absent, the system can be considered as a spinless system for which $\mathcal{T}$ is simply a complex conjugation operator. Therefore one can adopt a gauge for the Bloch functions such that $u^*_{n\mathbf{k}}(\mathbf{r}) = u_{n-\mathbf{k}}(\mathbf{r})$. On the other hand, inversion symmetry connects $u_{n\mathbf{k}}(-\mathbf{r})$ to $u_{n-\mathbf{k}}(\mathbf{r})$, and we are allowed to let $u_{n\mathbf{k}}(-\mathbf{r}) = u_{n-\mathbf{k}}(\mathbf{r})$. Combining the above two equations, one obtains $u^*_{n\mathbf{k}}(\mathbf{r}) = u_{n\mathbf{k}}(-\mathbf{r})$. Then it is straightforward to show that the corresponding effective Hamiltonian $H(\mathbf{k})$ has to be real-valued, i.e., $H_{mn}(\mathbf{k}) = H_{nm}(\mathbf{k})$.

A BT problem at an arbitrary $\mathbf{k}$ point can be minimally described by a two-band effective Hamiltonian, which can be expressed in terms of the identity matrix and the three Pauli matrices. According to the above argument, the two-band Hamiltonian for a system respecting both $\mathcal{T}$ and $\mathcal{P}$ symmetries can be chosen as real valued, so the codimension of such a BT problem is 2, one less than the number of independent variables (i.e., k_x, k_y and k_z). Hence a nodal loop is stable in the presence of coexisting $\mathcal{T}$ and $\mathcal{P}$ symmetries.

Some other symmetries of the system, such as C_2 rotation about the A-H line and C_3 rotation about the k_z axis, are crucial in determining the shape of the nodal loop. Nevertheless, the nodal loop would be robust even in the absence of these additional crystal symmetries; weakly breaking them would just distort the loop.

Effective Hamiltonian. We further construct a minimal effective Hamiltonian that can describe the nodal loop around the A point. We adopt a spinless two-band Hamiltonian of the form

$$h(\mathbf{q}) = \epsilon(\mathbf{q})\sigma_0 + \mathbf{d}(\mathbf{q}) \cdot \vec{\sigma}, \tag{1}$$

where the 2×2 identity matrix σ_0 and Pauli matrices $\vec{\sigma} = (\sigma_x, \sigma_y, \sigma_z)$ operate in the pseudospin space of the two bands that cross near the A point and $\mathbf{q} = \mathbf{k} - \mathbf{k}_A$. Since $\epsilon(\mathbf{q})\sigma_0$ represents an overall energy shift, we neglect this term in the following analysis.

Let us start by considering the symmetries of the systems which impose constraints on the allowed form of the coefficients $d_i(\mathbf{q})$ $(i = x, y, z)$. The little group at A contains a threefold rotation C_3 about k_z, a twofold rotation C_2 about the A-H axis, inversion

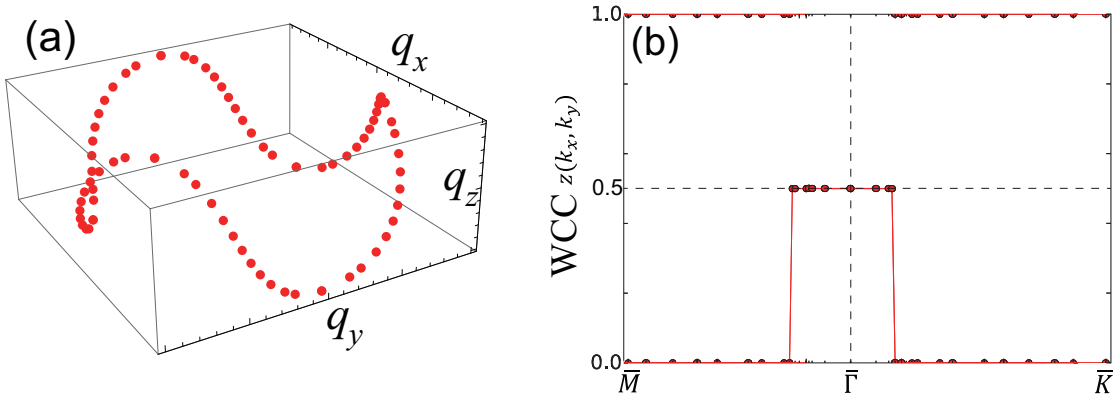

FIG. 3. (Color online) Calculated band touching points (nodal line) in 3D **k**-space using the effective Hamiltonian of Eqs. (1) and (2). (b) Evolution of Wannier charge center $z(k_x, k_y)$ for the occupied bands.

$\mathcal{P}$, and time reversal $\mathcal{T}$. Thus the Hamiltonian has to obey the symmetry constraints $U\,h(\mathbf{q})\,U^{-1} = h(U^{-1}\mathbf{q})$, for $U = C_3, C_2, \mathcal{P}$ and $\mathcal{T}$ [25].

First-principles calculations indicate that the low-energy states at the A point are mostly contributed by the Sn s and Sn p_z orbitals. If we choose the two basis vectors as $|s\rangle$ and $|p_z\rangle$, the symmetry operations of the little group take the form $C_3 = \sigma_0$, $C_2 = \sigma_z$, $\mathcal{P} = \sigma_z$ and $\mathcal{T} = K\sigma_0$. Then we obtain the symmetry-allowed expressions for $d_i(\mathbf{q})$:

$$\begin{aligned} d_x &= 0, \\ d_y &= Aq_z + B(q_x^2 q_y - q_x q_y^2) \\ &\quad + C(q_x^2 + q_y^2 - q_x q_y)q_z + Dq_z^3, \\ d_z &= M + E(q_x^2 + q_y^2 - q_x q_y) + Fq_z^2. \end{aligned} \tag{2}$$

We see from Eq. (2) that the Hamiltonian is expressed only in terms of two of the three Pauli matrices, which is consistent with the previous codimension argument.

In order to achieve a band crossing on the A-H line ($q_z = 0$), $ME < 0$ must be satisfied, which is nothing but the band-inversion condition. The A point lies within the band-inverted region, hence the two bands tend to cross each other as **k** moves away from A. Based on the effective Hamiltonian, we determine the BT points by solving the equations $\mathbf{d}(\mathbf{q}) = \mathbf{0}$. The calculated BT points form a snake-like ring around the A point as shown in Fig. 3(a), which is consistent with the iso-energy-surface calculation as shown in Fig. 2(b).

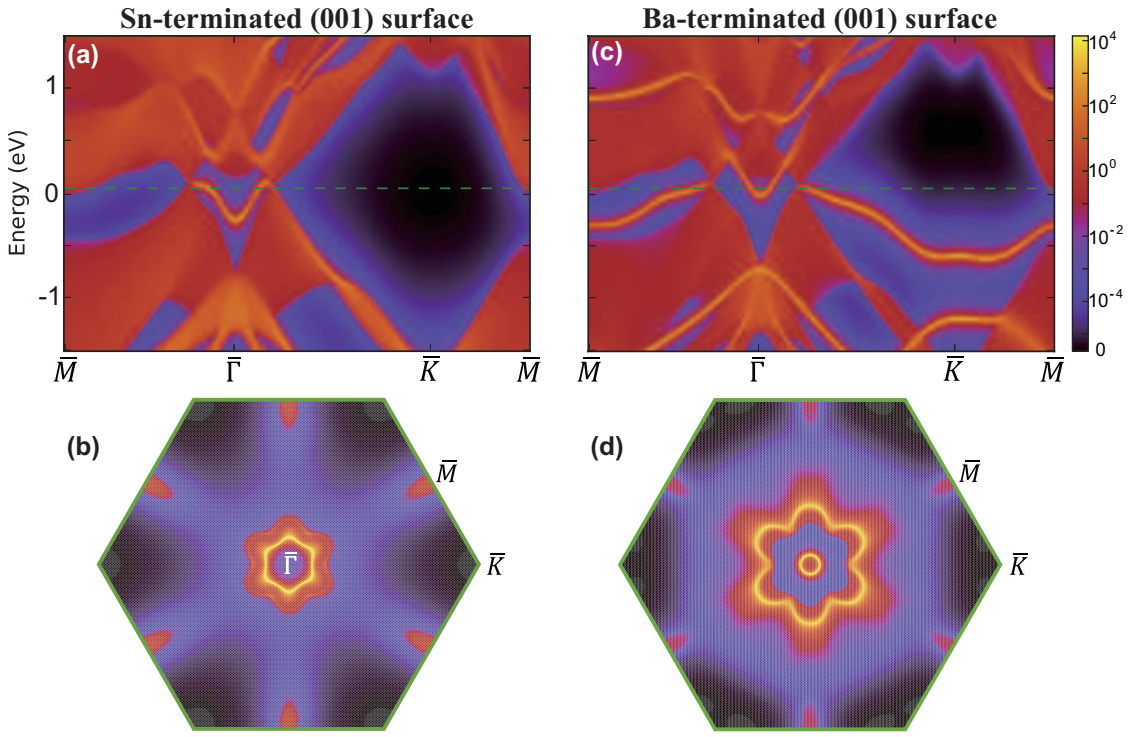

FIG. 4. (Color online) Calculated (001) surface band structure and Fermi surface without SOC for (a, b) Sn-terminated, and (c, d) Ba-terminated, surfaces. The Fermi surfaces shown in (b) and (d) are calculated with the chemical potential at 60 meV [green dashed lines in (a) and(c)]. Note that the inner circle in (d) originates from a concave conduction band state, not from the drumhead-like surface state.

Topological invariant. To identify the nontrivial band topology in $BaSn_2$, we further study the evolution of the 1D hybrid Wannier charge centers (WCCs) along a high-symmetry path in the k_x-k_y plane [22, 27–29]. The sum of the hybrid WCCs over the occupied subspace, $z(k_x, k_y)$ (in unit of c), is equivalent (up to a factor of 2π) to the total Berry phase of the occupied Bloch functions accumulated along the k_z direction. For a spinless system respecting both $\mathcal{T}$ and $\mathcal{P}$ symmetries, the Berry phase has to be either 0 or π for an arbitrary loop in the BZ. Therefore, we expect that the total hybrid WCC $z(k_x, k_y)$ would be quantized as either 0 or 1/2 at any (k_x, k_y), and that $z(k_x, k_y)$ would jump by 1/2 when passing through a projected nodal point. This is exactly what happens in $BaSn_2$ without SOC. As shown in Fig. 3(b), we find that $z(k_x, k_y)$ is 1/2 inside the projected nodal loop centered at $\bar{\Gamma}$ in the projected 2D Brillouin zone and jumps to zero outside, as is expected from the above discussions.

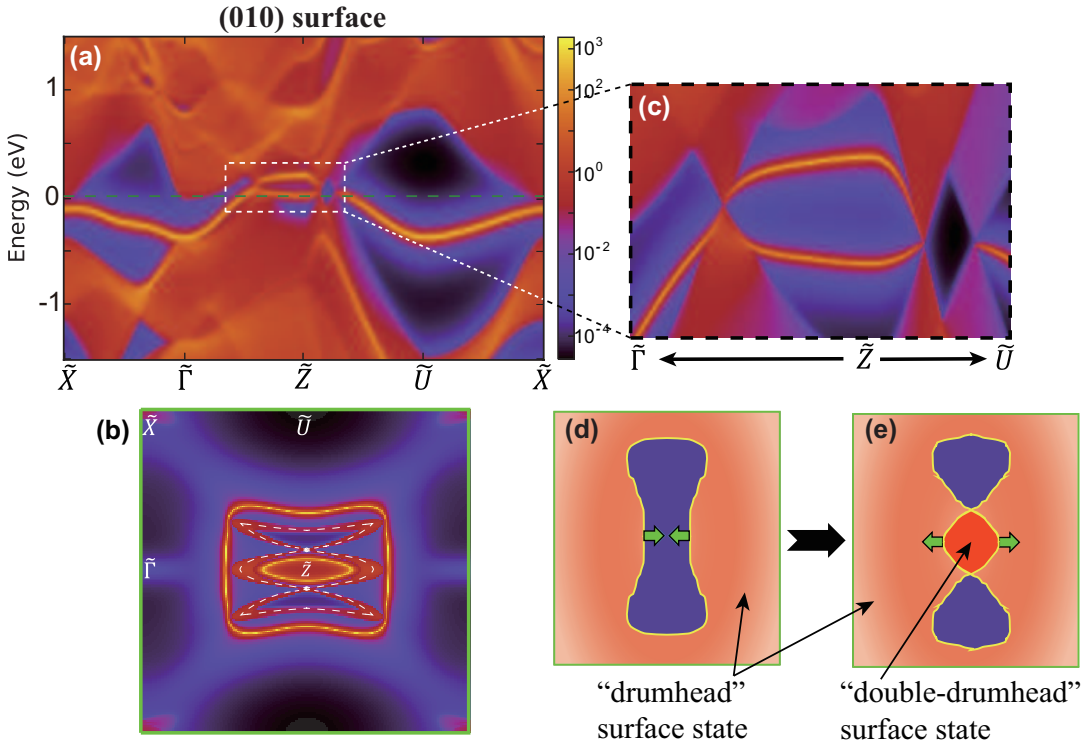

FIG. 5. (Color online) (a) Calculated (010) surface band structure and (b) Fermi surface without SOC. The Fermi surfaces shown in (b) are calculated with the chemical potential at 10 meV [green dashed lines in (a)]. The white dashed line in (b) forming an ellipse and two crescents indicates the projected nodal line on the (010) surface. Surface states exist outside the projected nodal loop and inside the ellipse. (c) Enlargement of the double drumhead-like (010) surface bands near $\tilde{Z}$. (d)-(e) Schematic illustration of the formation of "double-drumhead" surface states due to nodal loop twisting and intersecting.

Surface states. One of the most important signatures of a topological nodal-line semimetal is the existence of "drumhead-like" surface states either inside or outside the projected nodal loop [9, 12–14]. Figure 4 shows the calculated local density of states for the semi-infinite (001) surface, from which we have an intuitive visualization of surface band structure and Fermi surface. For the Sn-terminated (001) surface, the drumhead-like surface states are nestled inside the projected nodal loop as shown in Fig. 4(a)-(b). Unlike the nearly flat "drumhead" surface states in some previous works[12, 13], the surface states of $BaSn_2$ are more dispersive, with a bandwidth of about 180 meV. It is interesting to note that when the (001) surface is terminated on the Ba atomic layer, the topological surface states fill the

region outside the projected nodal loop as shown in Fig. 4(c)-(d), exactly the opposite as for the Sn-terminated surface. Such an interesting phenomenon stems from the properties of 1D atomic chains with $\mathcal{PT}$ symmetry, as explained in the supplement [25]. We have also checked that the local density of states of the surface states decays rapidly into the bulk and becomes negligible within five principal layers [25].

The surface states for the (010) surface are dramatically different. The interior region of the projected nodal loop now is divided into three subregions, one ellipse and two crescents [see Fig. 1(d) and the white dashed line in Fig. 5(b)]. As is shown in Fig. 5, there are two surface bands inside the ellipse, none inside the crescents, and one topological surface band outside the projected nodal loop. The single surface band outside the projected nodal loop is regarded as the hallmark of a bulk topological nodal-loop semimetal. On the other hand, the two surface bands inside the ellipse result from the twist and intersection of the projected nodal loop along the $\tilde{U}$-$\tilde{Z}$ line, so that the surface states outside the untwisted nodal loop [Fig. 5(d)] become overlaid with each other, leading to two drumhead-like surface states inside the ellipse [Fig. 5(e)].

SOC effect. In general, spin-orbit coupling (SOC) can drive the nodal-line semimetal into different topological phases, such as a topological insulator [30], 3D Dirac semimetal [13], or other kinds of nodal-line semimetals [14]. In graphene it is well known that SOC splits the BT, leading to a quantum spin Hall insulator [31]. Similarly, in a 3D system with a nodal loop, SOC generally lifts the degeneracy on the loop and drives the system into a 3D topological insulator [30]. Some crystalline symmetries, such as C_4 rotation or reflection, may protect the existence of the nodes at isolated $\mathbf{k}$ points or in a mirror plane, even in the presence of SOC, resulting in 3D Dirac semimetals [13] or nodal-line semimetals protected by crystalline symmetry [14].

In the case of $BaSn_2$, our first-principles calculations indicate that the SOC, which is much smaller than the dispersion of the nodal loop, completely lifts the degeneracy of the nodal loop, and a topological-insulator phase with a global energy gap of 13 meV results. We calculate the Z_2 invariants, finding, $(\nu_0; \nu_1\nu_2\nu_3) = (1; 001)$, and the Dirac surface states, thus identifying the nontrivial band topology [25]. We further check the SOC-induced gap along the nodal loop locally and find that the gap is $\sim$50 meV on the Γ-M-L-A plane, while it increases to a maximum value of $\sim$160 meV on the A-H line. Note that $BaSn_2$ is an extreme case among the AX_2 compounds, where both Ba and Sn are heavy elements with

relatively strong SOC.

The SOC strength may be diminished by doping or substituting lighter elements such as Si or Ca, potentially allowing the nodal-line semimetal topological-insulator phases to reappear. Our detailed investigations are reported in the Supplement [25]. Similar to $BaSn_2$, alkaline-earth stannides ($SrSn_2$ and $CaSn_2$), germanides ($BaGe_2$, $SrGe_2$ and $CaGe_2$) and silicides ($BaSi_2$ and $SrSi_2$) all exhibit nodal-line semimetal behaviors in the absence of SOC. Meanwhile, the SOC-induced splitting of the nodal line gets smaller from stannides to silicides ($< 10\,\mathrm{meV}$). Moreover, various new properties show up in these materials. For example, in addition to the nodal loop, isolated point nodes appear around the M point in $BaSi_2$, while unlike $BaSn_2$, there are only isolated nodes on the k_z axis in $CaSi_2$. More importantly, a type-II 3D Dirac-fermion electronic structure, which is robust against SOC, appears in the valence bands of most akaline-earth stannides and germanides. This new type of quasiparticle is a counterpart of the recently discovered type-II Weyl fermions [32], and is expected to exhibit novel properties distinct from previous Dirac semimetals. The details of this exotic type-II Dirac semimetal will be discussed in future work [33].

Conclusion. In summary, we have theoretically predicted the existence of 3D topological nodal-line semimetals in alkaline-earth compounds AX_2 when SOC is neglected. The single snake-like nodal loop distinguishes this class of materials from existing nodal-line semimetals which typically have multiple nodal rings. The drumhead-like surface states on the (001) surface may appear either inside or outside the projected nodal loop, depending on surface termination, while some unconventional double-drumhead-like surface states occur on the (010) surface. Including SOC drives the system into a topological-insulator phase whose Z_2 indices are (1;001). As the SOC effect is much weaker in alkaline-earth compounds composed of light elements, the nodal-line semimetal as and its exotic electronic properties are expected to be observed in these materials.

We thank Professor Hongbin Zhang for valuable discussions and fruitful suggestions. H. H. and W. D. are supported by the Ministry of Science and Technology of China (Grant Nos. 2011CB606405 and 2011CB921901) and the National Natural Science Foundation of China (Grant No. 11334006). J. L. and D. V. are supported by NSF Grant DMR-14-08838.

[1] M. Z. Hasan and C. L. Kane, Rev. Mod. Phys. **82**, 3045 (2010); X.-L. Qi and S.-C. Zhang, *ibid.* **83**, 1057 (2011).

[2] H. Huang, J. Liu, and W. Duan, Phys. Rev. B **90**, 195105 (2014).

[3] F. D. M. Haldane, Phys. Rev. Lett. **61**, 2015 (1988).

[4] C.-Z. Chang, J. Zhang, X. Feng, J. Shen, Z. Zhang, M. Guo, K. Li, Y. Ou, P. Wei, L.-L. Wang, *et al.*, Science **340**, 167 (2013).

[5] H. Zhang, H. Huang, K. Haule, and D. Vanderbilt, Phys. Rev. B **90**, 165143 (2014).

[6] H. Huang, Z. Liu, H. Zhang, W. Duan, and D. Vanderbilt, Phys. Rev. B **92**, 161115 (2015).

[7] Z. Wang, Y. Sun, X.-Q. Chen, C. Franchini, G. Xu, H. Weng, X. Dai, and Z. Fang, Phys. Rev. B **85**, 195320 (2012); Z. Wang, H. Weng, Q. Wu, X. Dai, and Z. Fang, *ibid.* **88**, 125427 (2013).

[8] H. Weng, C. Fang, Z. Fang, B. A. Bernevig, and X. Dai, Phys. Rev. X **5**, 011029 (2015); S.-M. Huang, S.-Y. Xu, I. Belopolski, C.-C. Lee, G. Chang, B. Wang, N. Alidoust, G. Bian, M. Neupane, C. Zhang, *et al.*, Nat. Commun. **6** (2015); B. Q. Lv, H. M. Weng, B. B. Fu, X. P. Wang, H. Miao, J. Ma, P. Richard, X. C. Huang, L. X. Zhao, G. F. Chen, Z. Fang, X. Dai, T. Qian, and H. Ding, Phys. Rev. X **5**, 031013 (2015); S.-Y. Xu, I. Belopolski, N. Alidoust, M. Neupane, G. Bian, C. Zhang, R. Sankar, G. Chang, Z. Yuan, C.-C. Lee, *et al.*, Science **349**, 613 (2015).

[9] A. A. Burkov, M. D. Hook, and L. Balents, Phys. Rev. B **84**, 235126 (2011).

[10] G. P. Mikitik and Y. V. Sharlai, Phys. Rev. B **73**, 235112 (2006); Low Temp. Phys. **34**, 794 (2008).

[11] T. T. Heikkilä and G. E. Volovik, JETP Lett. **93**, 59 (2011); New J. Phys. **17**, 093019 (2015).

[12] H. Weng, Y. Liang, Q. Xu, R. Yu, Z. Fang, X. Dai, and Y. Kawazoe, Phys. Rev. B **92**, 045108 (2015).

[13] R. Yu, H. Weng, Z. Fang, X. Dai, and X. Hu, Phys. Rev. Lett. **115**, 036807 (2015); Y. Kim, B. J. Wieder, C. L. Kane, and A. M. Rappe, **115**, 036806 (2015).

[14] G. Bian, T.-R. Chang, R. Sankar, S.-Y. Xu, H. Zheng, T. Neupert, C.-K. Chiu, S.-M. Huang, G. Chang, I. Belopolski, *et al.*, Nat. Commun. **7** (2016); G. Bian, T.-R. Chang, H. Zheng, S. Velury, S.-Y. Xu, T. Neupert, C.-K. Chiu, S.-M. Huang, D. S. Sanchez, I. Belopolski,

N. Alidoust, P.-J. Chen, G. Chang, A. Bansil, H.-T. Jeng, H. Lin, and M. Z. Hasan, Phys. Rev. B **93**, 121113 (2016).

[15] L. S. Xie, L. M. Schoop, E. M. Seibel, Q. D. Gibson, W. Xie, and R. J. Cava, APL Mater. **3**, 083602 (2015).

[16] Y.-H. Chan, C.-K. Chiu, M. Chou, and A. P. Schnyder, arXiv:1510.02759 (2015).

[17] S.-J. Kim and T. F. Fässler, Zeitschrift für Kristallographie-New Crystal Structures **223**, 325 (2008).

[18] R. C. Ropp, *Encyclopedia of the alkaline earth compounds* (Newnes, 2012).

[19] G. Kresse and J. Furthmüller, Comput. Mater. Sci. **6**, 15 (1996).

[20] P. E. Blöchl, Phys. Rev. B **50**, 17953 (1994).

[21] J. P. Perdew, K. Burke, and M. Ernzerhof, Phys. Rev. Lett. **77**, 3865 (1996).

[22] N. Marzari and D. Vanderbilt, Phys. Rev. B **56**, 12847 (1997); I. Souza, N. Marzari, and D. Vanderbilt, **65**, 035109 (2001).

[23] A. A. Mostofi, J. R. Yates, Y.-S. Lee, I. Souza, D. Vanderbilt, and N. Marzari, Comput. Phys. Commun. **178**, 685 (2008).

[24] M. P. López Sancho, J. M. López Sancho, and J. Rubio, J. Phys. F **14**, 1205 (1984); **15**, 851 (1985).

[25] See Supplementary Materials, http://link.aps.org/supplemental/xxx, for more details about the computational methods, the surface states, the effect of SOC, and the results of calculations of the electronic structures of other AX_2 compounds.

[26] R. M. Martin, *Electronic structure: basic theory and practical methods* (Cambridge university press, 2004).

[27] R. Yu, X. L. Qi, A. Bernevig, Z. Fang, and X. Dai, Phys. Rev. B **84**, 075119 (2011).

[28] A. A. Soluyanov and D. Vanderbilt, Phys. Rev. B **83**, 035108 (2011); **83**, 235401 (2011).

[29] M. Taherinejad, K. F. Garrity, and D. Vanderbilt, Phys. Rev. B **89**, 115102 (2014).

[30] A. Yamakage, Y. Yamakawa, Y. Tanaka, and Y. Okamoto, J. Phys. Soc. Jpn. **85**, 013708.

[31] C. L. Kane and E. J. Mele, Phys. Rev. Lett. **95**, 226801 (2005).

[32] A. A. Soluyanov, D. Gresch, Z. Wang, Q. Wu, M. Troyer, X. Dai, and B. A. Bernevig, Nature **527**, 495 (2015).

[33] H. Huang, W. Duan, *et al.*, In preparation.